nature communications

Article

https://doi.org/10.1038/s41467-024-48431-w

Spin-orbit torque manipulation of sub-terahertz magnons in antiferromagnetic α-Fe_2O_3

Received: 2 June 2023

Accepted: 1 May 2024

Published online: 14 May 2024

Check for updates

Dongsheng Yang[1,3], Taeheon Kim[1,2,3], Kyusup Lee[1], Chang Xu[1], Yakun Liu[1], Fei Wang[1], Shishun Zhao[1], Dushyant Kumar[1] & Hyunsoo Yang[1] ✉

The ability to electrically manipulate antiferromagnetic magnons, essential for extending the operating speed of spintronic devices into the terahertz regime, remains a major challenge. This is because antiferromagnetic magnetism is challenging to perturb using traditional methods such as magnetic fields. Recent developments in spin-orbit torques have opened a possibility of accessing antiferromagnetic magnetic order parameters and controlling terahertz magnons, which has not been experimentally realised yet. Here, we demonstrate the electrical manipulation of sub-terahertz magnons in the α-Fe_2O_3/Pt antiferromagnetic heterostructure. By applying the spin-orbit torques in the heterostructure, we can modify the magnon dispersion and decrease the magnon frequency in α-Fe_2O_3, as detected by time-resolved magneto-optical techniques. We have found that optimal tuning occurs when the Néel vector is perpendicular to the injected spin polarisation. Our results represent a significant step towards the development of electrically tunable terahertz spintronic devices.

Magnons, the quanta of collective spin-wave excitations, carry the spin angular momentum without moving charges[1,2], and could serve as potential information carriers, allowing Joule-heat-free data transfer, These features have made them of great interest in the energy-efficient information technology[3–5]. Antiferromagnets, where two-spin sublattices are aligned antiparallel due to the negative exchange interaction, host antiferromagnetic (AFM) magnons which have frequencies that are 2–3 orders of magnitude higher than their ferromagnetic counterparts due to a stronger AFM exchange energy[6,7], and insulating antiferromagnets have low magnetic dissipation[8]. These features have rendered insulating antiferromagnets as a promising platform for energy-efficient terahertz (THz) magnonics and optoelectronics.

Such devices require active electronic control of THz magnons. One such approach is to utilise current-induced spin-orbit torques (SOT)[9,10]. However, attention has principally been confined to manipulating the static magnetic state, leading to AFM magnetic reorientation/switching[11–14]. In stark contrast, the direct control of the THz spin dynamics in antiferromagnets, such as the magnon frequency, is critical for novel applications such as THz spin nano-oscillators[15–17] and rectifiers[18–21]. Pioneering efforts to control the magnon frequency have focused on conventional ferromagnetic and ferrimagnetic thin films and two-dimensional exfoliated flakes, whose magnon frequencies reside in tens of GHz[22–28]. Although theoretical works[15,17,29,30] pointed out that the frequency of the uniform resonant mode (wavevector $k = 0$ magnon) in antiferromagnets can be controlled by SOT, the experimental demonstration, including propagating magnons ($k \neq 0$), has remained elusive.

Here, we demonstrate the electrical control of the sub-THz magnon frequency in an easy-plane AFM insulator, α-Fe_2O_3. For this work, we use 5-mm-thick, (0001)-oriented α-Fe_2O_3 crystals (Fig. 1a, b). Figure 1c, d show the X-ray diffraction pattern and atomic force microscopy image of the α-Fe_2O_3 sample, respectively, confirming the high

---

[1]Department of Electrical and Computer Engineering, National University of Singapore, Singapore, Singapore. [2]Electro-Medical Device Research Centre, Korea Electrotechnology Research Institute, Ansan, Republic of Korea. [3]These authors contributed equally: Dongsheng Yang, Taeheon Kim.
✉e-mail: eleyang@nus.edu.sg

crystal quality and the [0001] crystallographic orientation. The magnetisation versus temperature is displayed in Fig. 2a. The magnetic phase transition in α-Fe_2O_3, called the Morin transition, occurs at the Morin temperature T_M, which is ~261 K. The magnetic configuration above T_M is schematically illustrated in Fig. 1b. The magnetic order of two sublattices, $\mathbf{m}_1$ and $\mathbf{m}_2$, is nearly antiparallel but slightly canted due

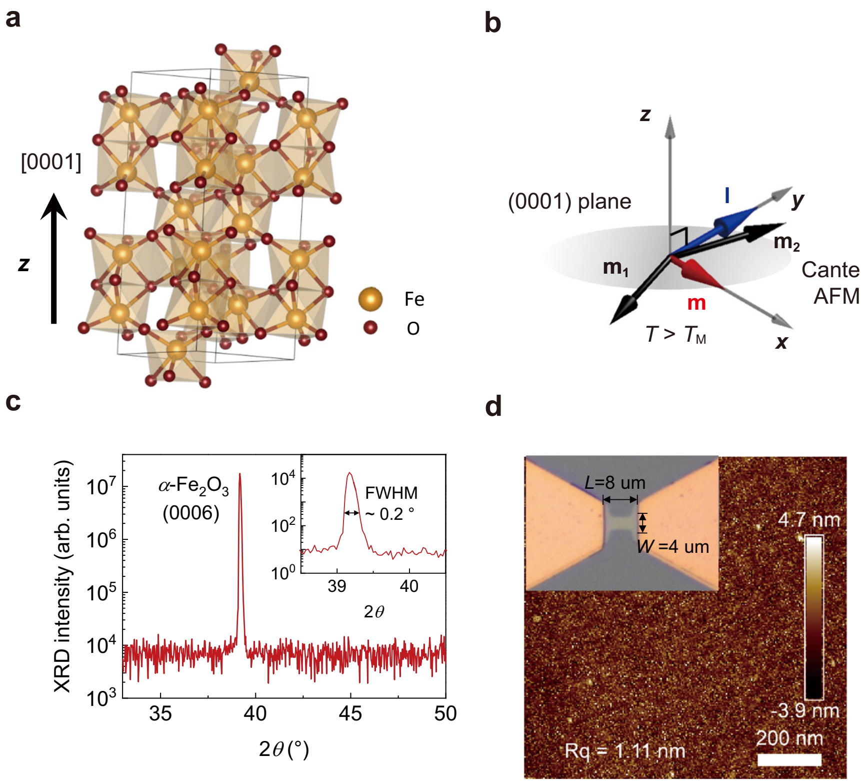

Fig. 1 | Material characterisation of α-Fe_2O_3 sample. a, **b** Crystal (**a**) and magnetic (**b**) structure of α-Fe_2O_3 above the Morin temperature $T_M = 261$ K. **m, l, $\mathbf{m}_1$** and **$\mathbf{m}_2$** represent a canted moment, Néel vector, and 1st and 2nd sublattice moment. **c** X-ray diffraction (XRD) measurement of the α-Fe_2O_3 sample. The peak at 39.2° matches well with the position of the α-Fe_2O_3 (0006) peak. Inset: the zoomed view of the α-Fe_2O_3 (0006) peak showing the full width at half maximum (FWHM). **d** Atomic force microscopy image of the α-Fe_2O_3 (0001) sample. The root mean square average (Rq) of the profile heights is 1.11 nm. Inset: the device image with a dimension of 4 μm in width (W) and 8 μm in length (L).

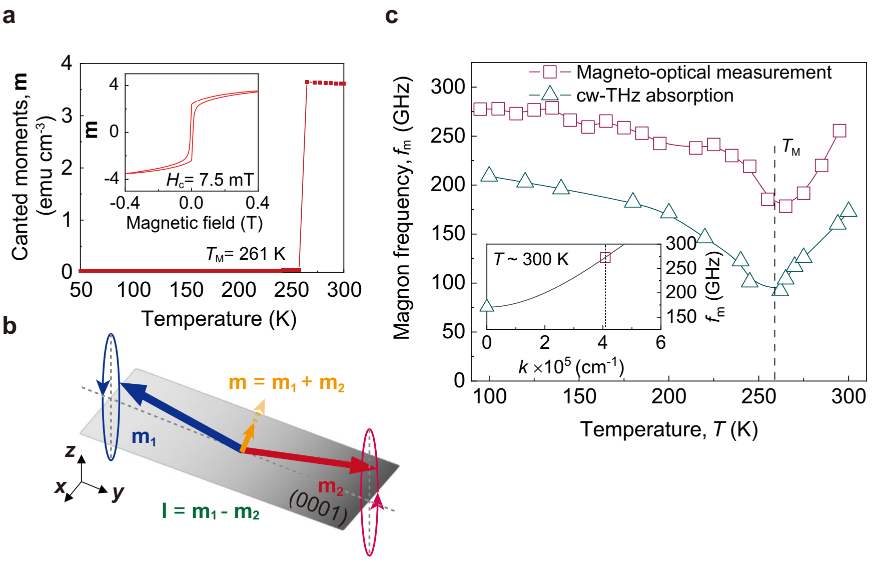

Fig. 2 | Temperature dependence of α-Fe_2O_3 magnon frequency f_m without applying currents. a Canted moments **m** as a function of temperature from 50 and 300 K, showing a Morin transition at T_M ~ 261 K. Inset: the magnetic hysteresis loop with an in-plane coercivity $H_c = 7.5$ mT at $T = 300$ K. **b** Configuration of q-AFM spin resonance. Both **l** and **m** are located in the (0001) plane and perpendicular to each other. **c** Temperature dependences of f_m (wavevector $k > 0$) obtained by magneto-optical measurement (squares) and f_m ($k = 0$) by continuous-wave terahertz (cw-THz) absorption measurement (triangles). The overall frequency blueshift measured by magneto-optical measurements is evidence of finite k magnons. Inset: the calculated α-Fe_2O_3 magnon dispersion relation for the q-AFM mode along the [0001] direction, in which both f_m and k match well with two measurement results.

to the Dzyaloshinskii-Moriya interaction (DMI)[31], resulting in a nearly unit-length Néel vector $\mathbf{l} = (\mathbf{m}_2 - \mathbf{m}_1)/2$ and a perpendicular canted magnetic moment $\mathbf{m} = (\mathbf{m}_1 + \mathbf{m}_2)/2$ and on the (0001) plane. The small coercivity around 7.5 mT (the inset of Fig. 2a) results from the insignificant in-plane magneto-anisotropy of α-Fe_2O_3. As a result, a weak external magnetic field (**H**) could align the direction of **m**, leading to a magnetic configuration with $\mathbf{l} \perp \mathbf{H}$ and $\mathbf{m} \,//\, \mathbf{H}$ in the (0001) plane. At room temperature, two eigenmodes of magnon in α-Fe_2O_3 correspond to the out-of-plane and in-plane elliptical precessional motion of $\mathbf{m}_1$ and $\mathbf{m}_2$ lying in the (0001) plane[32]. Our study focuses on the out-of-plane precessional mode, also known as the quasi-antiferromagnetic (q-AFM) mode, which exhibits sub-THz magnon frequencies (Fig. 2b)[33]. In contrast, the frequency of the in-plane mode, or the quasi-ferromagnetic (q-FM) mode, resides in the range of several GHz in the absence of **H**[34,35].

Results

Sub-THz magnon measurements in α-Fe_2O_3 with currents

In this work, we use the time-resolved magneto-optical method for observing the sub-THz magnons in α-Fe_2O_3 (Methods, Supplementary Note 1). This method is a benchmark technique to investigate the spin dynamics in AFM insulators through magneto-optical interactions, i.e., the Faraday effect and Cotton-Mouton effect. Specifically, the spin dynamics in α-Fe_2O_3 are obtained via ultrafast excitation of the pump pulse with the photon energy of 3.1 eV above the α-Fe_2O_3 bandgap and detected by tracking the polarisation rotation of the probe pulse using typical magneto-optical detection, similar to previous experiments[36–39] (Supplementary Notes 2 and 3). We adopt this method as it is sensitive to the interfacial effect where SOT tuning prevails and can measure higher-frequency magnon components with finite k[26,40].

To identify the value of magnon wavevector k measured by the time-resolved magneto-optical method, we first measure the resonance ($k = 0$ magnon) frequency by using a continuous-wave THz (cw-THz) absorption method (Supplementary Note 4)[41]. The temperature-dependent q-AFM magnon frequency f_m of α-Fe_2O_3 without the current using both methods are summarised in Fig. 2c. The results of cw-THz absorption method indicate a resonance frequency of approximately 200 GHz at room temperature with a dip in the vicinity of the T_M, which is consistent with the q-AFM resonance mode ($k = 0$ magnon) in α-Fe_2O_3[33]. In comparison, the f_m measured by the time-resolved magneto-optical method displays a similar trend but is consistently shifted by ~70 GHz over that by the cw-THz absorption method. This consistent blueshift in frequency constitutes concrete evidence for the existence of finite k magnons, similar to the previous report on AFM $DyFeO_3$[40]. In this case, the value of probed k can be determined using the Bragg equation[42] $k = 2k_0 n(\lambda_0)\cos\delta'$ in which k_0 is the wavenumber of the probe light, $n(\lambda_0)$ is the refractive index of α-Fe_2O_3/Pt heterostructure at the centre wavelength of the probe beam $\lambda_0 = 800$ nm and δ' is the refraction angle of the probe beam at an incidence angle δ. By applying our experimental parameters[43] with $n(\lambda_0)$ equating 2.6 at $\lambda_0 = 800$ nm and δ being 0°, the measured k in the time-resolved magneto-optical experiment is estimated to be $4.08 \times 10^5\,\mathrm{cm}^{-1}$ (Supplementary Note 5).

To quantitatively correlate the f_m with different k, the magnon dispersion of α-Fe_2O_3 along [0001] or the z direction (Supplementary Notes 6 and 7) is given by

$$f_m(k, J_c) = \sqrt{(\upsilon_0 k)^2 + f_{m,k=0}^2(J_c)}, \tag{1}$$

where $\upsilon_0 \sim 32\,\mathrm{km\,s^{-1}}$ is the limiting magnon velocity along the [0001] crystalline direction[44], $f_{m,k=0}$ is the q-AFM magnon frequency at $k = 0$, and J_c is the applied charge current. The value of f_m at $k = 4.08 \times 10^5\,\mathrm{cm}^{-1}$ is larger than that of $f_{m,k=0}$ as it is shifted by $\upsilon_0 k$. Here, λ_0 is dominant in determining k, whereas the δ dependence on k is small; $\delta = 0°$ ($\delta = 30°$) corresponds to $k = 4.08 \times 10^5\,\mathrm{cm}^{-1}$ ($k = 4 \times 10^5\,\mathrm{cm}^{-1}$) and $f_m = 272$ GHz ($f_m = 269$ GHz). As shown in the inset of Fig. 2c, both f_m and k extracted from both time-resolved magneto-optical and cw-THz absorption methods agree well with the calculated magnon dispersion, as a cross-check of the k value extracted by the Bragg equation. In addition, we observe a slow oscillation mode at ~55 GHz (Fig. 3). This corresponds to a laser-induced acoustic phonon mode, which has been widely studied previously[40,42] (Supplementary Note 8).

SOT manipulation of sub-THz α-Fe_2O_3 magnons

Next, we explore the SOT manipulation for the α-Fe_2O_3 magnons at $k = 4.08 \times 10^5\,\mathrm{cm}^{-1}$. As illustrated in Fig. 3a, the adjacent Pt is a strong spin-orbit coupling material and acts as the spin source. By applying J_c across the Pt layer, transverse spin accumulations are generated at the α-Fe_2O_3/Pt interface with the spin polarisation $\boldsymbol{\sigma}$. The spin accumulation induces a SOT on the magnetic order of α-Fe_2O_3 and generates magnon current density J_m, allowing for the manipulating of f_m. To understand the modified magnon dispersion, we adopt a magnon-mediated spin current J_m, which can propagate into α-Fe_2O_3 (Method and Supplementary Note 9). By monitoring the polarisation rotation of the reflected probe pulses under different J_c, the manipulation of the f_m can be studied as a function of J_c (Fig. 3b, c).

To confirm the dominant mechanism of SOT rather than other unwanted effects (e.g., heating and strain), we perform the measurements under both $\boldsymbol{\sigma} \,//\, \mathbf{m}$ and $\boldsymbol{\sigma} \,//\, \mathbf{l}$ configurations. Due to the large size of the magnetic domain in the α-Fe_2O_3 sample, which exceeds hundreds of micrometres, our device can be considered in a saturated mono-domain condition (Methods and Supplementary Fig. 13). Figure 3c, d summarises the f_m with different J_c and under both configurations ($\boldsymbol{\sigma} \,//\, \mathbf{l}$ and $\boldsymbol{\sigma} \,//\, \mathbf{m}$). The direction of **m** in α-Fe_2O_3 is aligned along the external magnetic field **H** and is orthogonal to the orientation of **l** in the (0001) plane, as confirmed by spin Hall magnetoresistance measurements (Supplementary Fig. 14). No magnetic field is applied during the time-resolved magneto-optical measurement.

At the $\boldsymbol{\sigma} \,//\, \mathbf{m}$ configuration, we observe that f_m decreases non-linearly with increasing J_c from 272 GHz at $J_c = 0\,\mathrm{A\,cm^{-2}}$ to 258 GHz at $J_c = 2 \times 10^7\,\mathrm{A\,cm^{-2}}$, resulting in a f_m tuning of −14 GHz (the minus sign refers to a redshift of f_m). We note that this redshift of f_m is opposite to the heating-induced effect that increases f_m when $T > T_M$. Moreover, we find that the tuning effect is symmetrical with the polarity of J_c, which is distinct from that of ferromagnets[26]. This is reasonable as J_c does not break the symmetry of **l** in α-Fe_2O_3[8]. Furthermore, we find that the frequency of the acoustic phonon f_p remains unchanged with J_c, which supports that the tuning of f_m is due to spin-related mechanisms rather than the strain resulting from the current flow. We further developed a comprehensive spin-wave model that combined the SOT and AFM magnon dispersion to explain our experimental observations (Supplementary Notes 7 and 8). In the $\boldsymbol{\sigma} \,//\, \mathbf{m}$ configuration, SOT reorients **l** from the equilibrium axis (the y-axis in Fig. 3d), reducing the effective anisotropy and finally resulting in the redshift of f_m. As shown in Fig. 3c, the simulation result in a solid line matches well with both the polarity dependence and the amount of f_m change.

We then study the second configuration with $\boldsymbol{\sigma} \,//\, \mathbf{l}$. As shown in Fig. 3c, we observe a similar redshifted trend in f_m by increasing the current density, with a reduced amount of −6 GHz tuning at $J_c = 2 \times 10^7\,\mathrm{A\,cm^{-2}}$, ~43% of that at $\boldsymbol{\sigma} \,//\, \mathbf{m}$. Therefore, f_m reveals distinct dependences on the configuration, showing that the direction of **l** with respect to $\boldsymbol{\sigma}$ is important for efficient f_m tuning. This anisotropic feature is analogous to the previous report on the α-Fe_2O_3 spin transport, where spins propagate longer with $\boldsymbol{\sigma} \,//\, \mathbf{l}$ than at $\boldsymbol{\sigma} \,//\, \mathbf{m}$[8]. Our result indicates that SOT is less pronounced at $\boldsymbol{\sigma} \,//\, \mathbf{l}$ than at $\boldsymbol{\sigma} \,//\, \mathbf{m}$, leading to a reduced f_m tuning. Furthermore, the simulated f_m at $\boldsymbol{\sigma} \,//\, \mathbf{l}$ in Fig. 3c matches the experimental results.

Discussion

To further confirm the role of SOT on the change in f_m, we conduct a control measurement in the α-Fe_2O_3/Cu (5 nm) device, where we have

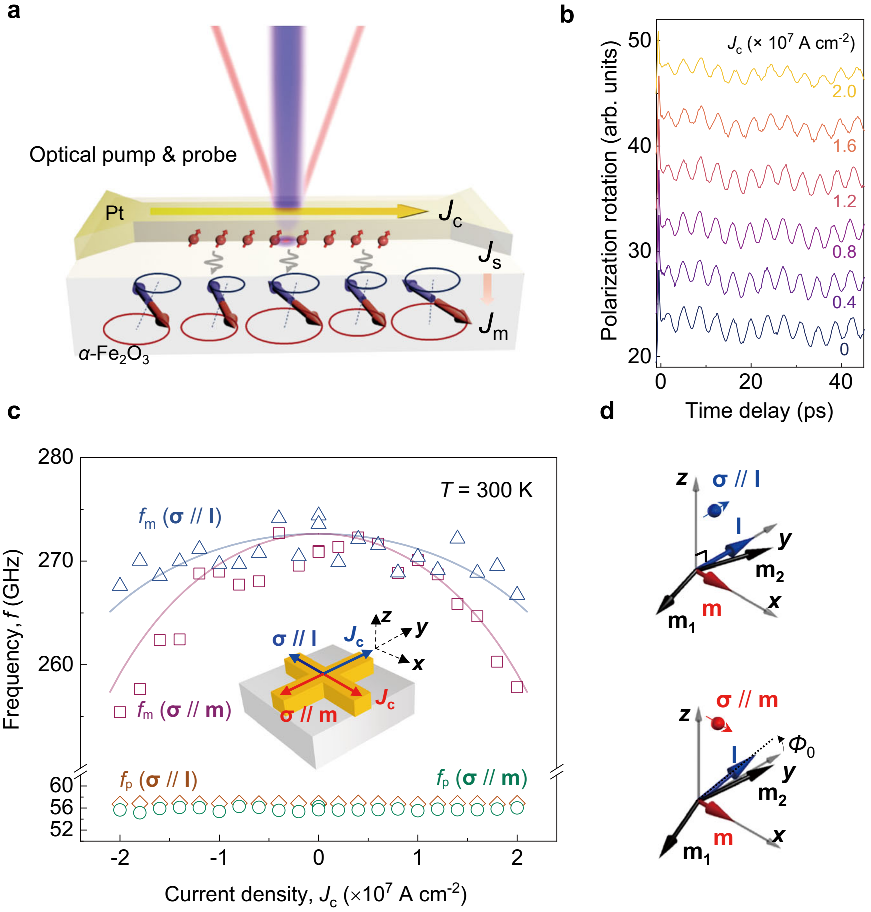

Fig. 3 | Experimental observation of SOT-manipulated q-AFM f_m of α-Fe$_2$O$_3$ at $T = 300$ K. **a** Schematics of the SOT-tuned AFM magnon measurement using the time-resolved magneto-optical method (Methods). Coherent magnons in α-Fe$_2$O$_3$ are excited via femtosecond optical pumping and manifest the polarisation rotation of the probe beam via magneto-optical interaction. J_c, J_s, and J_m are the injected charge current, spin current and magnon current, respectively. **b** f_m is manipulated by J_s injected from the adjacent Pt layer and detected as the oscillation signal using a balanced detection scheme (**σ** // **m** configuration). **σ**: spin polarisation. The overlapped phonon oscillation at phonon frequency $f_p = 55$ GHz can be used to judge SOT tuning. **c** Summary of SOT-tuned f_m and f_p with J_c at both **σ** // **l** and **σ** // **m** configurations. f_m at **σ** // **l** (**σ** // **m**) is denoted by triangles (squares) and f_p at **σ** // **l** (**σ** // **m**) is denoted by diamonds (circles). The solid lines represent the theoretical calculation results (Supplementary Note 7). **d** SOT-manipulated spin configurations at **σ** // **l** and **σ** // **m**, where Φ_0 is SOT-induced reorientation of **l**.

used Cu, due to its negligible spin-orbit coupling strength. No change is observed in f_m at either **σ** // **m** or **σ** // **l** configuration (Fig. 4a). These results confirm the SOT origin of our observed f_m tuning in Fig. 3c and rule out other strain and heating effects. Next, we consider the current-induced heating effect. The limited temperature rise may slightly increase f_m at $T > T_M$ (Fig. 2c) but cannot account for the observed decrease of f_m in Fig. 3c (Supplementary Note 10). Therefore, we conclude that SOT dominates the magnon tuning in our experiments. Figure 4b summarises the tunability and f_m in various magnetic materials by electrical means (Supplementary Table 1 for details). The SOT effect on the spin lifetime in Supplementary Note 11 shows no change for both spin configurations as the applied current density is smaller than that for self-oscillation.

Noticeably, tuning f_m using SOT is significantly more energy efficient compared to current-induced Oersted fields, H_{Oe}. The induced H_{Oe}, by Ampère's law ($H_{Oe} \sim \mu_0 J_C t_{Pt}/2$) is as small as $H_{oe} = 0.63$ mT for $J_c = 2 \times 10^7$ A cm^{-2}, where μ_0 is the vacuum permeability and t_{Pt} is the thickness of Pt layer. The f_m change induced by H_{Oe} is expected to be $\gamma H_{Oe}/2\pi \approx 0.017$ GHz, where γ is the electron gyromagnetic ratio, which is nearly 10^3 times smaller in magnitude than the manipulation of f_m achieved by SOT.

We calculate the magnon dispersion relation at **σ** // **m** as a function of J_c and plot in Fig. 4c (Supplementary Notes 6 and 7). As J_c increases, the dispersion relation curves near the $k = 0$ are redshifted downward. However, the amount of frequency shift at large k is smaller. Therefore, maximised frequency tuning occurs for the resonant mode ($k = 0$), resulting in a frequency tunability of −24 GHz/(2×10^7 A cm^{-2}). The SOT increases the band curvature and thus increases the magnon group velocity, $\upsilon_g = 2\pi \times \partial f_m/\partial k$. As shown in Fig. 4d, for $k = 4.08 \times 10^5$ cm^{-1} magnons, υ_g increases from 25.3 to 26.7 km s^{-1} at $J_c = 2 \times 10^7$ A cm^{-2} with **σ** // **m**. Furthermore, we explore the SOT-induced f_m modulation with varying the exchange field H_E and effective magnetic anisotropy field $H_{eff,K}$ for **σ** // **m** (Supplementary Note 12). In this case, antiferromagnets with a high H_E and low $H_{eff,K}$ are preferred for efficient f_m tuning, which is in line with the theoretical result that IrMn with a much higher $H_{eff,K} \sim 5000$ Oe yields a reduced tuning efficiency[45].

As shown in Fig. 4b, our work marks the electrically manipulated f_m at the highest frequency (270 GHz for $k = 4.08 \times 10^5$ cm^{-1} and 170 GHz for $k = 0$) ever reported. For magnetic materials with various values of f_m, it is fair to compare their tuning efficiency, defined as $\eta(J_c) = [f_m(J_c) - f_m(0)]/[J_c \times f_m(J_c)]$, under a normalised input amplitude. The efficiency of our α-Fe$_2$O$_3$/Pt heterostructure $\eta_{Fe2O3} = -6.8\%/(10^7$ A cm$^{-2})$ is more than five times higher than the benchmark ferrimagnetic yttrium iron garnet (YIG) with $\eta_{YIG} \sim -1.1\%/(10^7$ A cm$^{-2})$[22]. The magnetic field dependence of f_m in the same α-Fe$_2$O$_3$ sample is also measured. No clear change in f_m is observed up to 0.2 T magnetic field (Supplementary Note 13). This further supports the effectiveness of

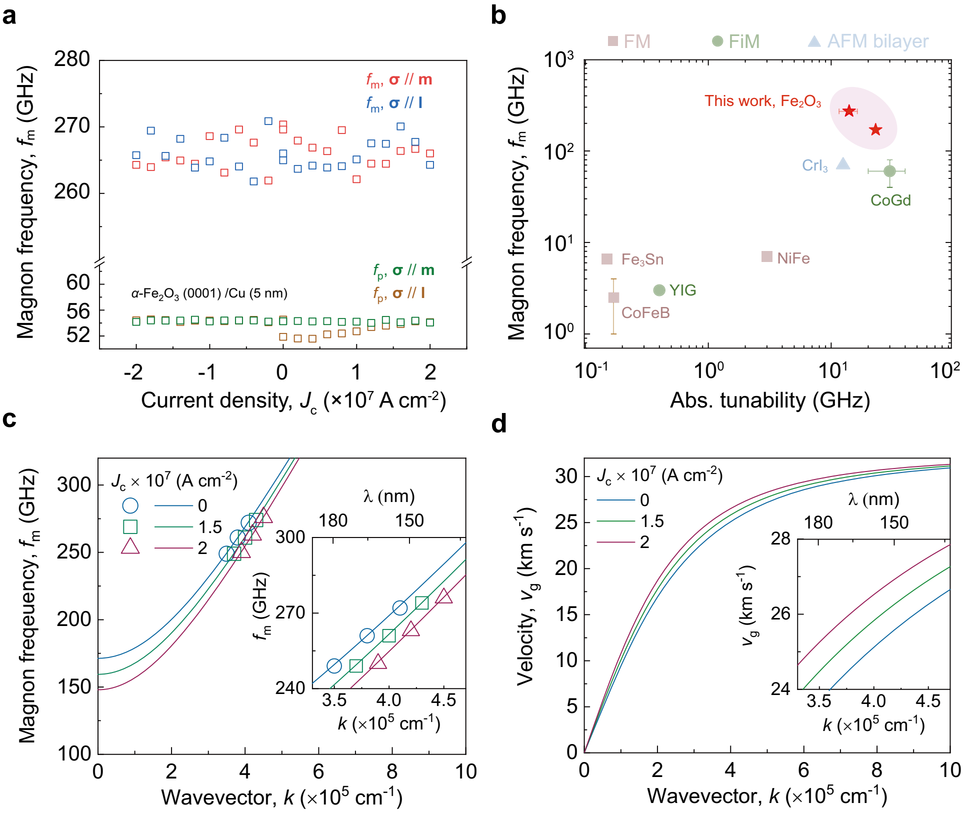

Fig. 4 | Control measurement of α-Fe$_2$O$_3$/Cu (5 nm) and simulation results of SOT-tuned α-Fe$_2$O$_3$ magnon dispersion. a Current-dependence of f_m and f_p in the controlled α-Fe$_2$O$_3$ (0001)/Cu (5 nm) device under two-spin configurations. Neither f_m nor f_p is tuned by J_c at both spin configurations, which suggests that SOT is essential for the observed f_m tuning in Fig. 3. **b** Comparison of the tunability and f_m by electrical means summarised in Supplementary Table 1. Two red stars represent f_m our tuning results for $k = 0$ and $k = 4.08 \times 10^5\,\text{cm}^{-1}$. The error bars indicate the uncertainty of the data extracted from references. FM: ferromagnet, FiM: Ferrimagnet, AFM: antiferromagnet. **c** Numerical (symbols) and analytical (lines) calculated magnon dispersion in the **σ** // **m** configuration. Maximum f_m tunability of −23 GHz occurs for the zone centre (resonant) mode at $J_c = 2 \times 10^7\,\text{A cm}^{-2}$. **d** Magnon group velocity with k extracted from **c**. The magnon group velocity increases effectively for intermediate k, leading to an increase from 25.3 to 26.7 km s^{-1} at $J_c = 2 \times 10^7\,\text{A cm}^{-2}$ for $k = 4.08 \times 10^5\,\text{cm}^{-1}$.

the SOT-tuning in α-Fe$_2$O$_3$ magnon. Although other stimuli such as strain[46], Joule heating[23,47] and magnetic fields[3] can potentially realise a similar or even greater tunability, the application scenarios are severely limited by their substantial energy consumption and poor device scalability. SOT-tuning requires only a nanometre-thick spin source, which is a critical feature for the miniaturisation of future spintronic devices.

Our work provides an efficient and universal means to manipulate sub-THz magnons electrically in antiferromagnets. The SOT manipulation of magnons is applicable to a wide range of AFM materials without utilising exotic spin textures or complicated device structures. It, therefore, can play a significant role in developing all-electrical THz magnonic and photonic devices. For example, it can be used to create on-chip integrated THz photonics nano-circuits[48].

Methods

(0001) cut α-Fe$_2$O$_3$ single crystal

The α-Fe$_2$O$_3$ single-crystalline sample with a thickness of 1 mm was purchased from MaTeck Material-Technologie & Kristalle GmbH (Germany). The sample surface was polished with a surface roughness of about 1 nm and a miscut orientation angle below 0.1°.

Device fabrication

Prior to device fabrication, the α-Fe$_2$O$_3$ sample surface was cleaned with acetone, isopropyl alcohol (IPA) and deionised (DI) water by a standard ultrasonic bath process. A maskless ultraviolet lithography system (TTT-07-UVlitho, TuoTuo Technology (Singapore) Pte. Ltd) was used for device patterning with channel dimensions of 4 μm wide and 8 μm long for subsequent deposition (inset of Fig. 1d). The Pt layer was deposited on α-Fe$_2$O$_3$ with a thickness of 5 nm using DC magnetron sputtering at a base pressure of 9×10^{-9} Torr. A 4 nm-thick SiO$_2$ insulating layer was deposited to protect the device from oxidation.

Spin Hall magnetoresistance measurements

In response to an external field, the orientations of magnetic order in α-Fe$_2$O$_3$ are coupled with spin currents injected from the adjacent Pt layer via the spin Hall effect, manifesting the spin Hall magnetoresistance (SMR)[49]. The AC longitudinal harmonic signals for Hall bar devices were measured in a physical property measurement system (PPMS, Quantum Design) at room temperature. During the measurement, a constant amplitude sinusoidal current with a frequency of 13.7 Hz was applied to the devices by a Keithley 6221 current source. The angle-dependent first-harmonic longitudinal voltage V_f was recorded by a Stanford research SR830 lock-in amplifier to obtain the first-harmonic longitudinal resistance R_f while rotating the in-plane magnetic field of 1 T. The negative sign of SMR with a value of $\Delta R/R \sim 0.2\,\%$ indicates an excellent interfacial quality of spin injection into α-Fe$_2$O$_3$ (Supplementary Note 14).

Time-resolved magneto-optical measurements

In the time-resolved magneto-optical setup, the probe beam was the output of an 80 MHz Ti: sapphire femtosecond laser system (Spectra-Physics Mai Tai, pulse duration of 75 fs) centred at 1.55 eV (800 nm), and the pump beam was the second harmonic by using a β-Barium borate single crystal to 3.1 eV (400 nm). Both pump and probe pulses were linearly polarised. The fluence ratio between the pump and probe beams was around 10:1. Both beams were focused onto the sample surface at normal incidence by a ×50 objective lens (the pump beam diameter is ~1.8 μm with a typical fluence of 1.0 mJ cm^{-2}; the probe beam diameter is ~1.2 μm with a typical fluence of 100 μJ cm^{-2}). The magnon detection depth is the order of the penetration length of probe beams in α-Fe_2O_3, which is around 300 nm[50]. In this case, the reduced amplitude of SOT away from the α-Fe_2O_3/Pt interface potentially leads to the broadening of linewidth and reduced amplitude of magnon spectra in the magneto-optical results (Supplementary Note 15). A continuous flow cryostat system (ST-300, Janis) was used to set the sample temperature between 77 and 300 K with fluctuations below 0.1 K. For the applied current, square-wave-liked current pulses (a pulse amplitude: 0-4 mA; a pulse width: 20 μs; duty cycle: 2%) were generated by using a current source (Keithley 6221) and synchronised with the femtosecond laser beams through a function generator (DS345, Stanford Research). Reflectivity and the polarisation rotation of the probe beams were measured by using a Wollaston prism and a balanced detector combination (Supplementary Fig. 1). To be noted, the pure magnetic linear birefringence cannot be demodulated by using an HWP. However, in cases where both magnetic linear birefringence and dichroism simultaneously manifest, both the polarisation and ellipticity of the probe beam become subject to tuning. In such circumstances, the oscillating signal emanating from magnons can be detected through the utilisation of either an HWP or by strategically manipulating the optical axis of a Wollaston prism.

In order to excite α-Fe_2O_3 magnons efficiently, a 400 nm (3.1 eV) femtosecond pulse is used for pumping. The optical radiation with photon energy larger than the bandgap (2.14 eV)[50] of α-Fe_2O_3 induces the strong electronic transition from O^{2-} to Fe^{3+} ions[51] (Supplementary Note 2). The spin excitation, mediated by the intense electronic transition, is strongly confined near the surface due to a finite penetration depth (~29 nm) of the pump light. Therefore, the spatially non-uniform and transient excitation ignites broadband magnons[40]. The oscillation signal of the manipulated magnons is detected by the polarisation rotation of the probe beam via the magnetic-optical interactions. It occurs due to the different refractive indices of the probe between the one parallel to the **l** and the other perpendicular to it on the α-Fe_2O_3 (0001) plane, which shows a sinusoidal signal as a function of the polarisation angle of probe light (Supplementary Fig. 4b). The limitation of the measurement scheme is that the thermal effect disturbs the magnon signal at higher $J_c > 2\times10^7$ A cm^{-2}, which prevents from conducting any meaningful analysis (details are shown in Supplementary Note 16). Therefore, we restrict the data analysis to $J_c < 2\times10^7$ A cm^{-2} in this work.

Magnetic domain measurement

At room temperature, we measure the magnetic domain of the α-Fe_2O_3(0001) single crystal using magneto-optical Kerr microscopy. Longitudinal geometry is employed to probe the canted in-plane magnetic moment of α-Fe_2O_3(0001). Similar to the earlier report[8], we observe distinct magnetic domains with a domain size over hundreds of micrometres (Supplementary Note 17). As this domain size much exceeds the size of SOT-tuned devices, it is reasonable to consider the main results under mono-domain conditions.

Atomistic spin simulations for α-Fe_2O_3 magnon

We construct an atomistic Landau-Lifshitz-Gilbert equation, including the damping-like SOT

$$\partial \mathbf{m}_i/\partial t = -\gamma \mathbf{m}_i \times \mathbf{H}_{\mathrm{eff},i} + \beta \mathbf{m}_i \times \partial \mathbf{m}_i/\partial t + J_{m,z} \mathbf{m}_i \times (\mathbf{m}_i \times \boldsymbol{\sigma}), \quad (2)$$

where $\mathbf{m}_i$ is the unit vector of magnetisation at site i, $\mathbf{H}_{\mathrm{eff},i}$ is the effective field, and $\boldsymbol{\sigma}$ is the spin polarisation. We use the following parameters of α-Fe_2O_3 at room temperature: the exchange field $H_E = 930$ T, the hard-axis anisotropy field $H_{Kz} = -16.8$ mT, the basal anisotropy field $H_B = 1$ μT, which originates from spontaneous magnetostriction[52], the Dzyaloshinskii-Moriya field $H_D = 2.5$ T, and $\gamma = 1.76\times10^{11}$ T s^{-1}. $J_{m,z}$ is the magnon spin current injected from Pt (Supplementary Note 9). To verify the dispersion relation, we apply an external ac magnetic field $H_{ext} = 10\ \mathrm{mT} \times \mathrm{sinc}(2\pi f t)$ and spatially distribute the magnetic field $H_{ext} = 0.1\ \mathrm{mT} \times \mathrm{sinc}(k(z\text{-}z_0))$ for the ignition of broadband magnons where z_0 is the surface of α-Fe_2O_3 and magnons propagate along the z direction. The DC magnon spin current is applied to the entire AFM system with the polarisation along the x and y directions. Numerical simulations were conducted from 0 to 1 μs with a minimum time interval of 0.1 ps with 10,000 spins. Magnon spin current is applied over a distance from 0 to 150 nm. The same parameters are used in theoretical and numerical calculations.

Data availability

All other data that support the plots within this paper and other findings of this study are available from the Supplementary Note or the corresponding author upon reasonable request.

Code availability

The code that has been used for this work is available from the corresponding author upon reasonable request.

References

1. Barman, A. et al. The 2021 magnonics roadmap. *J. Phys. Condens. Matter.* **33**, 413001 (2021).
2. Pirro, P., Vasyuchka, V. I., Serga, A. A. & Hillebrands, B. Advances in coherent magnonics. *Nat. Rev. Mater.* **6**, 1114–1135 (2021).
3. Li, J. et al. Spin current from sub-terahertz-generated antiferromagnetic magnons. *Nature* **578**, 70–74 (2020).
4. Kimel, A. V. et al. Ultrafast non-thermal control of magnetisation by instantaneous photomagnetic pulses. *Nature* **435**, 655–657 (2005).
5. Vaidya, P. et al. Subterahertz spin pumping from an insulating antiferromagnet. *Science* **368**, 160–165 (2020).
6. Kurihara, T., Bamba, M., Watanabe, H., Nakajima, M. & Suemoto, T. Observation of terahertz-induced dynamical spin canting in orthoferrite magnon by magnetorefractive probing. *Commun. Phys.* **6**, 51 (2023).
7. Caspers, C., Gandhi, V. P., Magrez, A., De Rijk, E. & Ansermet, J.-P. Sub-terahertz spectroscopy of magnetic resonance in $BiFeO_3$ using a vector network analyser. *Appl. Phys. Lett.* **108**, 241109 (2016).
8. Lebrun, R. et al. Tunable long-distance spin transport in a crystalline antiferromagnetic iron oxide. *Nature* **561**, 222–225 (2018).
9. Liu, L. et al. Spin-torque switching with the giant spin Hall effect of tantalum. *Science* **336**, 555–558 (2012).
10. Miron, I. M. et al. Perpendicular switching of a single ferromagnetic layer induced by in-plane current injection. *Nature* **476**, 189–193 (2011).
11. Takeuchi, Y. et al. Chiral-spin rotation of non-collinear antiferromagnet by spin-orbit torque. *Nat. Mater.* **20**, 1364–1370 (2021).
12. Chen, X. et al. Electric field control of Néel spin-orbit torque in an antiferromagnet. *Nat. Mater.* **18**, 931–935 (2019).
13. Peng, S. et al. Exchange bias switching in an antiferromagnet/ferromagnet bilayer driven by spin-orbit torque. *Nat. Electron.* **3**, 757–764 (2020).
14. Higo, T. et al. Perpendicular full switching of chiral antiferromagnetic order by current. *Nature* **607**, 474–479 (2022).
15. Cheng, R., Xiao, D. & Brataas, A. Terahertz antiferromagnetic spin Hall nano-oscillator. *Phys. Rev. Lett.* **116**, 207603 (2016).
16. Khymyn, R., Lisenkov, I., Tiberkevich, V., Ivanov, B. A. & Slavin, A. Antiferromagnetic THz-frequency Josephson-like oscillator driven by spin current. *Sci. Rep.* **7**, 43705 (2017).
17. Lee, D. K., Park, B. G. & Lee, K. J. Antiferromagnetic oscillators driven by spin currents with arbitrary spin polarisation directions. *Phys. Rev. Appl.* **11**, 054048 (2019).

18. Khymyn, R., Tiberkevich, V. & Slavin, A. Antiferromagnetic spin current rectifier. *AIP Adv* **7**, 055931 (2017).
19. Gomonay, O., Jungwirth, T. & Sinova, J. Narrow-band tunable terahertz detector in antiferromagnets via staggered-field and antidamping torques. *Phys. Rev. B* **98**, 104430 (2018).
20. Safin, A., Nikitov, S., Kirilyuk, A., Tyberkevych, V. & Slavin, A. Theory of antiferromagnet-based detector of terahertz frequency signals. *Magnetochemistry* **8**, 26 (2022).
21. Consolo, G. et al. Theory of the electric field controlled antiferromagnetic spin Hall oscillator and detector. *Phys. Rev. B* **103**, 134431 (2021).
22. Collet, M. et al. Generation of coherent spin-wave modes in yttrium iron garnet microdiscs by spin-orbit torque. *Nat. Commun.* **7**, 10377 (2016).
23. Divinskiy, B., Chen, G., Urazhdin, S., Demokritov, S. O. & Demidov, V. E. Effects of spin-orbit torque on the ferromagnetic and exchange spin-wave modes in ferrimagnetic CoGd alloy. *Phys. Rev. Appl.* **14**, 044016 (2020).
24. Zhang, X.-X. et al. Gate-tunable spin waves in antiferromagnetic atomic bilayers. *Nat. Mater.* **19**, 838–842 (2020).
25. Ishibashi, K. et al. All-optical probe of magnetisation precession modulated by spin-orbit torque. *Appl. Phys. Lett.* **117**, 122403 (2020).
26. Lyalin, I., Cheng, S. & Kawakami, R. K. Spin-orbit torque in bilayers of kagome ferromagnet Fe_3Sn_2 and Pt. *Nano Lett.* **21**, 6975–6982 (2021).
27. Ganguly, A. et al. Time-domain detection of current controlled magnetisation damping in Pt/$Ni_{81}Fe_{19}$ bilayer and determination of Pt spin Hall angle. *Appl. Phys. Lett.* **105**, 112409 (2014).
28. Salikhov, R. et al. Coupling of terahertz light with nanometre-wavelength magnon modes via spin-orbit torque. *Nat. Phys.* **19**, 529–535 (2023).
29. Mitrofanova, A., Safin, A., Kravchenko, O., Nikitov, S. & Kirilyuk, A. Optically initialised and current-controlled logical element based on antiferromagnetic-heavy metal heterostructures for neuromorphic computing. *Appl. Phys. Lett.* **120**, 072402 (2022).
30. Popov, P. et al. Voltage-controlled anisotropy and current-induced magnetisation dynamics in antiferromagnetic-piezoelectric layered heterostructures. *Phys. Rev. Appl.* **13**, 044080 (2020).
31. Shiino, T. et al. Antiferromagnetic domain wall motion driven by spin-orbit torques. *Phys. Rev. Lett.* **117**, 087203 (2016).
32. Han, J. et al. Birefringence-like spin transport via linearly polarised antiferromagnetic magnons. *Nat. Nanotechnol.* **15**, 563–568 (2020).
33. Grishunin, K., Mashkovich, E., Kimel, A., Balbashov, A. & Zvezdin, A. Excitation and detection of terahertz coherent spin waves in antiferromagnetic α-Fe_2O_3. *Phys. Rev. B* **104**, 024419 (2021).
34. Boventer, I. et al. Room-temperature antiferromagnetic resonance and inverse spin-Hall voltage in canted antiferromagnets. *Phys. Rev. Lett.* **126**, 187201 (2021).
35. Wang, H. et al. Spin pumping of an easy-plane antiferromagnet enhanced by Dzyaloshinskii-Moriya interaction. *Phys. Rev. Lett.* **127**, 117202 (2021).
36. Miwa, S. et al. Giant effective damping of octupole oscillation in an antiferromagnetic Weyl semimetal. *Small Sci.* **1**, 2000062 (2021).
37. Kampfrath, T. et al. Coherent terahertz control of antiferromagnetic spin waves. *Nat. Photon.* **5**, 31–34 (2011).
38. Satoh, T. et al. Spin oscillations in antiferromagnetic NiO triggered by circularly polarised light. *Phys. Rev. Lett.* **105**, 077402 (2010).
39. Zheng, Z. et al. Magneto-optical probe of ultrafast spin dynamics in antiferromagnetic CoO thin films. *Phys. Rev. B* **98**, 134409 (2018).
40. Hortensius, J. et al. Coherent spin-wave transport in an antiferromagnet. *Nat. Phys.* **17**, 1001–1006 (2021).
41. Moriyama, T. et al. Intrinsic and extrinsic antiferromagnetic damping in NiO. *Phys. Rev. Mater.* **3**, 051402 (2019).
42. Takahara, M., Jinn, H., Wakabayashi, S., Moriyasu, T. & Kohmoto, T. Observation of coherent acoustic phonons and magnons in an antiferromagnet NiO. *Phys. Rev. B* **86**, 094301 (2012).
43. Querry, M. R. *Optical Constants*. *Report No*. D-A158-D-A623 (University of Missouri, 1985).
44. Samuelsen, E. J. & Shirane, G. Inelastic neutron scattering investigation of spin waves and magnetic interactions in α-Fe_2O_3. *Phys. Status Solidi B* **42**, 241–256 (1970).
45. Safin, A. et al. Electrically tunable detector of THz-frequency signals based on an antiferromagnet. *Appl. Phys. Lett.* **117**, 222411 (2020).
46. Haykal, A. et al. Antiferromagnetic textures in $BiFeO_3$ controlled by strain and electric field. *Nat. Commun.* **11**, 1704 (2020).
47. Demidov, V. E. et al. Control of magnetic fluctuations by spin current. *Phys. Rev. Lett.* **107**, 107204 (2011).
48. Baumgaertl, K. et al. Nanoimaging of ultrashort magnon emission by ferromagnetic grating couplers at GHz frequencies. *Nano Lett.* **20**, 7281–7286 (2020).
49. Nakayama, H. et al. Spin Hall magnetoresistance induced by a nonequilibrium proximity effect. *Phys. Rev. Lett.* **110**, 206601 (2013).
50. Marusak, L. A., Messier, R. & White, W. B. Optical absorption spectrum of hematite, α-Fe_2O_3 near IR to UV. *J. Phys. Chem. Solids* **41**, 981–984 (1980).
51. Galuza, A., Beznosov, A. & Eremenko, V. Optical absorption edge in α-Fe_2O_3: The exciton-magnon structure. *Low Temp. Phys.* **24**, 726–729 (1998).
52. Morrish, A. H. *Canted Antiferromagnetism: Hematite*. (World Scientific, 1994).

Acknowledgements

The research was supported by the National Research Foundation (NRF) Singapore Investigatorship (NRFI06-2020-0015).

Author contributions

Y.L. and D.Y. fabricated the devices. D.Y., F.W. and D.K. performed material characterisations. D.Y. and K.L. performed the time-resolved experiments. D.Y., K.L. and T.K. analysed the data. T.K. performed the theoretical and numerical calculations. C.X. conducted simulations for current-induced heating. S.Z. conducted static MOKE measurements. H.Y. conceived the experiments and supervised the project. All authors contributed to the writing of the manuscript.

Competing interests

The authors declare no competing interests.

Additional information

Supplementary information The online version contains supplementary material available at https://doi.org/10.1038/s41467-024-48431-w.

Correspondence and requests for materials should be addressed to Hyunsoo Yang.

Peer review information *Nature Communications* thanks the anonymous reviewers for their contribution to the peer review of this work. A peer review file is available.

Reprints and permissions information is available at http://www.nature.com/reprints

Publisher's note Springer Nature remains neutral with regard to jurisdictional claims in published maps and institutional affiliations.

Open Access This article is licensed under a Creative Commons Attribution 4.0 International License, which permits use, sharing, adaptation, distribution and reproduction in any medium or format, as long as you give appropriate credit to the original author(s) and the source, provide a link to the Creative Commons licence, and indicate if changes were made. The images or other third party material in this article are included in the article's Creative Commons licence, unless indicated otherwise in a credit line to the material. If material is not included in the article's Creative Commons licence and your intended use is not permitted by statutory regulation or exceeds the permitted use, you will need to obtain permission directly from the copyright holder. To view a copy of this licence, visit http://creativecommons.org/licenses/by/4.0/.

© The Author(s) 2024